Nonhydrostatic Atmospheric Modeling Using a Combined Cartesian Grid

Hiroe Yamazaki and Takehiko Satomura

Division of Earth and Planetary Sciences, Graduate School of Science, Kyoto University, Kyoto, Japan

ABSTRACT

A new method for representing topography on a Cartesian grid is applied to a two-dimensional nonhydrostatic atmospheric model to achieve highly precise simulations over steep terrain. The shaved cell method based on finite-volume discretization is used along with a cell-combining approach in which small cut cells are combined with neighboring cells either vertically or horizontally. A unique staggered arrangement of variables enables quite simple computations of momentum equations by avoiding the evaluation of surface pressure and reducing the computational cost of combining cells for the velocity variables. The method successfully reproduces flows over a wide range of slopes, including steep slopes where significant errors are observed in a model using conventional terrain-following coordinates. The advantage of horizontal cell combination on extremely steep slopes is also demonstrated.

1. Introduction

The conventional terrain-following approach to simulate atmospheric flows over topography is to discretize the governing equations on a grid that conforms to the lower boundary. The main advantage of this approach is that the imposition of the lower boundary condition is greatly simplified. However, horizontal gradient computation on a terrain-following grid is essentially subject to truncation errors due to nonorthogonal coordinates (e.g., Thompson et al. 1985; Zängl 2003). In the presence of steep topography, the slantwise intersection of grid lines renders computational inaccuracy of advection and diffusion terms (e.g., Schär et al. 2002; Zängl 2002). In addition, imbalances in the discretization of the horizontal pressure gradient leads to artificial circulations around steep slopes, which affect local dynamics near mountains (e.g., Sundqvist 1976; Janjić 1989). Most nonhydrostatic models introduce reference profiles to reduce the errors associated with terrain-following coordinates (e.g., Klemp and Wilhelmson 1978; Satomura 1989; Tomita and Satoh 2004). However, truncation errors around steep slopes are still expected to be large under windy conditions (Steppeler et al. 2006). For example, Satomura

(1989) demonstrated that truncation errors due to nonorthogonal coordinates are visualized as discontinuities in mountain waves simulated over a semicircular mountain by his terrain-following model. Since an increase in horizontal resolution introduces steep slopes over mountainous areas, the terrain-following approach is no longer considered accurate enough for ultra-high-resolution simulations, which will gain popularity with the use of next-generation supercomputers.

A fundamental solution to this long-standing issue of the terrain-following approach is to keep model levels horizontal and discretize the governing equations on a Cartesian grid. One way to incorporate the effect of arbitrary topography into a Cartesian grid is to use the step mountain method (e.g., Bryan 1969; Mesinger et al. 1988). This approach approximates topography by a piecewise constant function along the grid lines that allows straightforward imposition of boundary conditions on the ground surface. On the other hand, the stepwise approximation of topography introduces serious problems in flow simulation. Gallus and Klemp (2000), for example, showed that vertical velocity errors occur over the corners of mountain steps, resulting in distortion of mountain waves. They also indicated that the step mountain method suffers from a "wind sheltering" problem: wind is strongly underestimated in the lee sides of mountains. According to Steppeler et al. (2006), this problem is potentially more serious because Gallus and Klemp (2000) report that the underestimation of winds does not decrease when the

---

Corresponding author address: Hiroe Yamazaki, Division of Earth and Planetary Sciences, Graduate School of Science, Kyoto University, Sakyo, Kyoto 606-8502, Japan.
E-mail: yamazaki_h@kugi.kyoto-u.ac.jp

vertical grid spacing is substantially reduced. The partial cell method is similar to the step mountain method except that the heights of the steps are adjusted to those of the topography (e.g., Semtner and Mintz 1977). It also has the same problem due to its stepwise structure that inevitably stands out around steep slopes where the topographic height varies largely in a horizontal grid length.

A different approach to Cartesian coordinate modeling is based on approximating topography by a piecewise linear function or quadratic function. This approach is popular in computational fluid dynamics (CFD) and is referred to as the immersed boundary method (Mittal and Iaccarino 2003). Clearly, the immersed boundary method represents a smoother and more precise boundary surface than step mountain method. However, the imposition of boundary conditions is complicated since the immersed boundary does not coincide with the grid lines. A number of methods have been proposed to impose boundary conditions on the immersed boundary through direct or indirect means.

The immersed boundary method has also been used in some geophysical fluid dynamics (GFD) models. For example, Tseng and Ferziger (2003) applied the immersed boundary method to an ocean model using a finite-difference approach to impose boundary conditions on the immersed boundary. They defined "ghost" computational points inside the topography, and imposed the boundary condition by extrapolating the variable to a ghost point and using it in standard finite-difference discretization. Though their method has the advantage of easy implementation into models with low computational costs, it is not designed to satisfy conservation laws in the vicinity of the immersed boundary. To preserve the model's conservation properties, it is suitable to use a finite-volume approach.

Immersed boundary schemes with finite-volume discretization are referred to as the cut cell method in CFD and have been used to simulate various flows with stationary and moving boundaries (e.g., Udaykumar et al. 1996, 2001; Ye et al. 1999; Mittal et al. 2003). In GFD models, another method very similar to the cut cell method is used. It was originally developed by Adcroft et al. (1997) for simulating ocean flows with irregular geometry, and is referred to as the shaved cell method. This method was applied to simulate atmospheric flows by Steppeler et al. (2002). They showed that the method did not suffer from the problems reported by Gallus and Klemp (2000) in the step mountain method. Yamazaki and Satomura (2008) demonstrated that shaved cell method is effective in reducing errors in terrain-following models due to slantwise intersection of grid lines.

A disadvantage in using the shaved cell or cut cell method is that small cells cut by the immersed boundary require small time steps to satisfy the Courant–Friedrichs–Lewy (CFL) condition. It is especially crucial for GFD models to avoid this severe restriction on time steps in order to keep the computational time reasonable.

As a remedy to the small cell problem, Steppeler et al. (2002) used the "thin wall" approximation, in which the computational volumes of all cut cells are artificially increased to those of uncut cells. They developed a two-dimensional nonhydrostatic atmospheric model using the thin-wall approximation and showed acceptable results in some mountain-wave simulations. Some internal inconsistency occurs due to the expansion of volumes while keeping the surface areas fixed (Lock 2008). Also, there are situations where the solution is unsatisfactory (Walko and Avissar 2008). Steppeler et al. (2006) converted the two-dimensional model into a three-dimensional model, called the z-coordinate version of the Lokalmodell (LM-z), and compared it with the terrain-following version of the Lokalmodell (LM-tf) in the case of precipitation forecasts over real topography. They found that the threat score and RMSE are better in LM-z. Because the thin-wall approximation was not entirely introduced to LM-z, no systematic model comparison with regard to the effect of volume expansion has been reported yet.

As an alternative to the thin-wall approximation, Walko and Avissar (2008) recommended the method used by Calhoun and LeVeque (2000), which is not yet implemented in their Ocean–Land–Atmosphere Model (OLAM). In this method, inward and outward fluxes of cut cells are implicitly balanced, which enables the use of time steps corresponding to regular cells as in models using the thin-wall approximation. It is also true for this method that internal inconsistency is unavoidable, because artificial alteration of the computational cell volumes is required for certain shapes of cells.

Another issue in shaved cell modeling is handling cut cells whose center is underground, such as those marked with triangles in Fig. 1. A straight way to obtain reasonable solutions for those cells is to relocate the positions of the cell centers to the center of gravity of the fluid part in the cell. This approach is impractical in the present context because it requires very complicated interpolation procedures owing to the nonuniform structure of cell centers and thus is computationally too expensive for GFD models. Without relocating processes, OLAM prognoses the approximate solutions of solid-center cells by assuming that the cell volumes and cell areas are uniformly occupied by small solids. Though this approach has the advantage of easy achievement of momentum conservation, the assumption makes the shape of topography indistinct and impacts the flow dynamics near the immersed boundary.
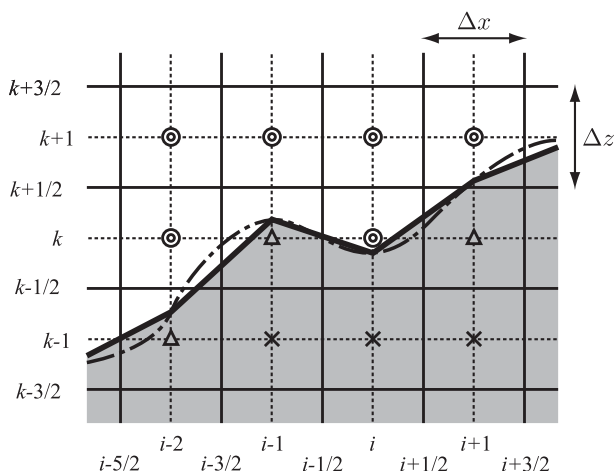
FIG. 1. Cartesian grids in the presence of topography. Dashed–dotted line and thick line describe the real topography and immersed boundary, respectively. Shaded region represents the topography in the model. Double circles and triangles represent fluid centers and solid centers, respectively. Cells marked with crosses are completely under the slope.

Here, we developed a two-dimensional nonhydrostatic atmospheric model using Cartesian coordinates for simulating flows over steep terrain, code-named "Sayaca-2D." To achieve both, sufficient accuracy of the lower boundary representation and reasonable consumption of computer resources, the shaved cell method is used along with a cell-combining technique in which small cut cells are combined with neighboring cells either vertically or horizontally. The use of combined cells provides two important advantages to represent topographical boundaries. One is that it avoids severe restriction by CFL criteria maintaining the rigid evaluation of cut cell volumes and thus avoids internal inconsistency. The other advantage is that there are no cut cells with solid centers, since such cells are absorbed by a neighboring cell during the combining procedure. The use of horizontal combinations in this paper is one of the main differences from the method in Yamazaki and Satomura (2008), which uses vertical combinations only. Horizontal combinations are particularly effective for extremely steep slopes that cross several model levels in a horizontal grid length where algorithms with only vertical combinations may form vertically long combined cells along the slopes and thus result in serious reduction of resolution.

The cut cell method in Ye et al. (1999) shares some features with the current method, particularly in terms of using combined cells. Their method requires the pressure values on the immersed boundary to calculate the pressure gradient at cut cells. The evaluation of surface pressure complicates the numerical algorithm for GFD simulations because zero gradient boundary condition

on the pressure field does not hold true for density-stratified flow. In addition, since geophysical flow is driven by slight perturbations of the pressure from the hydrostatically balanced state, extrapolation of the pressure perturbation to the surface could affect the flow dynamics near the immersed boundary. Our method enables simple pressure gradient calculations near the boundary without the evaluation of surface pressure by introducing a unique staggered arrangement of variables. This arrangement of variables makes another difference from Yamazaki and Satomura (2008) that uses a standard C-staggered grid (Arakawa and Lamb 1977) and approximates the pressure gradient on a combined cell by that on the upper part of the cell.

Numerical examples of mountain waves are given in section 3. The test problem of flow over a semicircular mountain conducted by Satomura (1989) is simulated properly by Sayaca-2D. The advantage of horizontal cell combination on extremely steep slopes is also demonstrated using a cliff with slopes over 80°.

2. Model description

a. Governing equations

In this study, fully compressible quasi-flux-form equations, developed by Satomura and Akiba (2003) are used. They are given by the following conservation equations for momentum, potential temperature, and mass:

$$\frac{\partial \rho u}{\partial t} = -\frac{\partial \rho uu}{\partial x} - \frac{\partial \rho uw}{\partial z} - \frac{\partial p'}{\partial x} + D_u, \tag{1}$$

$$\frac{\partial \rho w}{\partial t} = -\frac{\partial \rho wu}{\partial x} - \frac{\partial \rho ww}{\partial z} - \frac{\partial p'}{\partial z} - \rho' g + D_w, \tag{2}$$

$$\frac{\partial p'}{\partial t} = -\frac{c_p R}{c_v}\left(\frac{p}{p_0}\right)^{R/c_p}\left(\frac{\partial \rho \theta u}{\partial x} + \frac{\partial \rho \theta w}{\partial z} - D_\theta\right), \tag{3}$$

$$\frac{\partial \rho'}{\partial t} = -\frac{\partial \rho u}{\partial x} - \frac{\partial \rho w}{\partial z}, \tag{4}$$

and the equation of state:

$$\theta = \frac{p}{\rho R}\left(\frac{p_0}{p}\right)^{R/c_p}. \tag{5}$$

In these equations, u and w are the horizontal and vertical components of velocity, respectively; θ is the potential temperature; g is the acceleration due to gravity; p and ρ are the total pressure and total density, respectively; and the prime indicates deviations from the hydrostatically balanced state. Here c_p and c_v are the specific heats at constant pressure and constant volume,
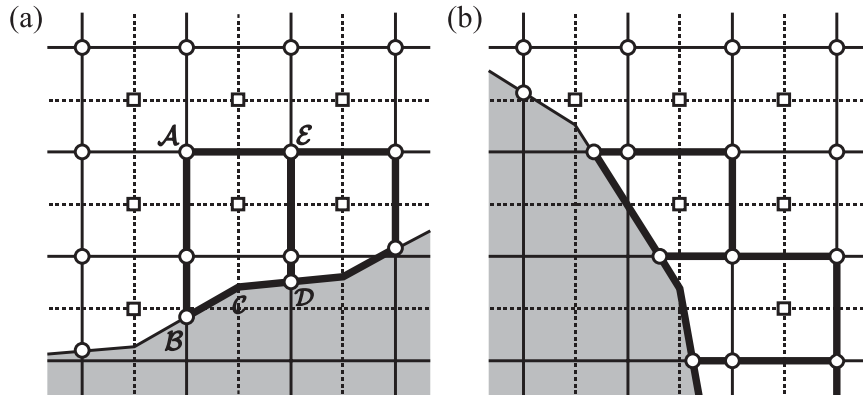
FIG. 2. Cell combination and variable arrangement. Thick lines describe the boundaries of combined cells. Squares and circles represent scalar points and velocity points, respectively. Shaded region represents the topography in the model. (a) Scalar cells on gentle slopes. (b) Scalar cells on steep slopes.

respectively; R is the gas constant; and p_0 is a reference pressure of 10^5 Pa. The terms D_u, D_w, and D_θ represent sources due to mixing and diffusion. Note that flux-form equations are well suited to finite-volume discretization in view of the conservation characteristics.

b. Grid configuration

Figure 1 illustrates Cartesian grids with spacing Δx and Δz in the presence of topography. In the current method, terrain heights are defined at the center of the grid column and approximated by a piecewise linear function, indicated by a thick line. Based on this representation of the immersed boundary, we identify cells cut by the immersed boundary and determine the intersections of the immersed boundary with the faces of these cells.

Next, cut cells whose center is underground or whose volume is smaller than or equal to $\Delta x \Delta z / 2$ are combined with a neighboring cell either vertically or horizontally. The direction of cell combination is determined by mean slope angle σ, which is evaluated for each cut cell as

$$\sigma_{i,k} = \tan^{-1}\left(\frac{h_{i+1/2} - h_{i-1/2}}{\Delta x}\right), \qquad (6)$$

where $h_{i+1/2}$ and $h_{i-1/2}$ are the terrain heights at $i + \frac{1}{2}$ and $i - \frac{1}{2}$, respectively.

Here we assume that the range of σ is $(-\pi/2, \pi/2)$. If $|\sigma| \leq \tan^{-1}(\Delta z/\Delta x)$, the above cut cells are combined with each upper cell; otherwise, they are combined with either each right or left cell with a fluid center. This procedure forms vertically combined cells on gentle slopes and horizontally combined cells on steep slopes as shown in Figs. 2a and 2b, respectively. After this combination, the computational volumes of all cells become larger

than half of a regular cell. Here, we assume that the topography is well resolved on the grid, and are not concerned with an extremely steep v-shaped valley or a very narrow sharp-pointed mountain.

The arrangement of the variables is an important aspect of the current method. In the case of Fig. 2, scalar variables and velocity components are arranged on the points of squares and circles, respectively. Scalar variables are arranged on the cell centers. Velocity components are arranged on the corners of the cells, except for the corners of cell faces fitted to the immersed boundary, such as point $\mathcal{C}$. This unique arrangement of variables enables quite simple computation of momentum equations, as discussed in detail in the following section.

The vertical grid staggering used here is classified by Thuburn and Woollings (2005) as their "category 5" configuration. They found that discretizations in this category suffered from such problems as having multiple computational modes, unstable modes and modes which could not be identified as any known physical mode. However, most cut cell methods used in CFD use a collocated grid, which belongs to configurations of the same category and give good results for various simulations (e.g., Udaykumar et al. 1996, 2001; Ye et al. 1999; Mittal et al. 2003). In section 3 our method also reproduces sufficiently accurate flows over a wide range of slopes from a gently sloping bell-shaped mountain to an extremely steep cliff. Therefore, it is supposed that our method still allows for acceptable results for flows over various terrain shapes.

c. Spatial discretization

Equations (1)–(4) are discretized in space using the finite-volume method. The idea of finite-volume discretization is based on Gauss's divergence theorem, which
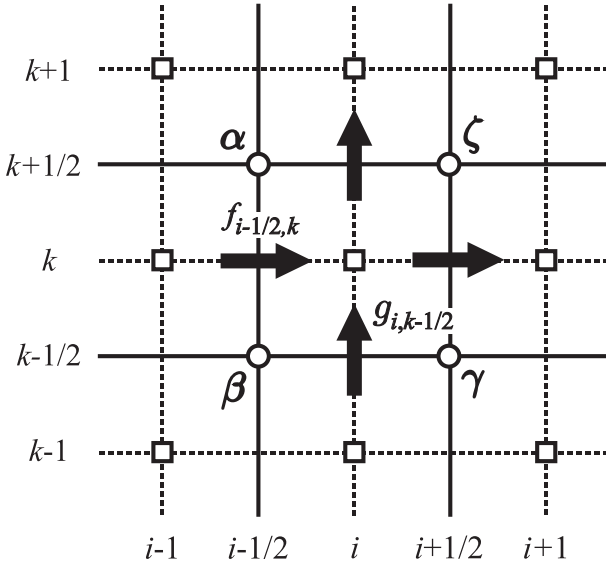
FIG. 3. Flux calculation on an uncut scalar cell. Squares and circles represent scalar points and velocity points, respectively. Arrows indicate fluxes at the face centers.

states that the volume integral of the vector divergence over a control volume is transformed to the surface integral of the flux across the control surface:

$$\int_{cv} \nabla \cdot \mathbf{f} \, dV = \oint_{cs} \mathbf{f} \cdot \mathbf{n} \, dS, \qquad (7)$$

where cv and cs denote the control volume and control surface, respectively; $\mathbf{n}$ is a unit vector normal to the control surface; and $\mathbf{f} = (f, g)$ is the flux vector. The finite-volume method assumes that the vector divergence is constant over a control volume. Rearranging Eq. (7), the vector divergence through a cell (i, k) can be expressed as

$$(\nabla \cdot \mathbf{f})_{i,k} = \frac{1}{V_{i,k}} \oint_{cs} \mathbf{f} \cdot \mathbf{n} \, dS, \qquad (8)$$

where $V_{i,k}$ is the volume of the cell.

Starting with the simplest case, consider an uncut cell with four corners, α, β, γ, and ζ (Fig. 3). The surface integral is computed over the four faces of the cell as

$$\oint_{cs} \mathbf{f} \cdot \mathbf{n} \, dS = \int_{\zeta\gamma} f \, dz - \int_{\alpha\beta} f \, dz + \int_{\alpha\zeta} g \, dx - \int_{\beta\gamma} g \, dx. \qquad (9)$$

To estimate these integrals on the faces to second-order accuracy, the midpoint rule can be used, which requires

the evaluation of the integrand at the center of the face. Supposing that $\mathbf{f}$ is advective flux $\mathbf{f} = \phi \mathbf{u}$, where ϕ is the scalar quantity, the integrals on the left face and the bottom face of the cell are approximated as

$$\int_{\alpha\beta} f \, dz \approx f_{i-(1/2),k} \overline{\alpha\beta} = \overline{\phi}^x_{i-(1/2),k} \overline{u}^z_{i-(1/2),k} \Delta z, \qquad (10)$$

$$\int_{\beta\gamma} g \, dx \approx g_{i,k-(1/2)} \overline{\beta\gamma} = \overline{\phi}^z_{i,k-(1/2)} \overline{w}^x_{i,k-(1/2)} \Delta x, \qquad (11)$$

respectively, where

$$\overline{\psi}^x_{i,k} \equiv [\psi_{i-(1/2),k} + \psi_{i+(1/2),k}]/2, \qquad (12)$$

$$\overline{\psi}^z_{i,k} \equiv [\psi_{i,k-(1/2)} + \psi_{i,k+(1/2)}]/2, \qquad (13)$$

and $\overline{\alpha\beta}$ and $\overline{\beta\gamma}$ indicate the lengths of the face $\alpha\beta$ and $\beta\gamma$, respectively. The integrals on the right face and the top face are calculated in the same way. Consequently, the divergence of the advective flux for the scalar quantity is discretized as

$$(\nabla \cdot \mathbf{f})_{i,k} = \frac{1}{V_{i,k}} [\overline{\phi}^x_{i+(1/2),k} \overline{u}^z_{i+(1/2),k} \Delta z - \overline{\phi}^x_{i-(1/2),k} \overline{u}^z_{i-(1/2),k} \Delta z$$
$$+ \overline{\phi}^z_{i,k+(1/2)} \overline{w}^x_{i,k+(1/2)} \Delta x - \overline{\phi}^z_{i,k-(1/2)} \overline{w}^x_{i,k-(1/2)} \Delta x] \qquad (14)$$

$$= \frac{1}{V_{i,k}} [\delta_x (\overline{\phi}^x \overline{u}^z)_{i,k} \Delta z + \delta_z (\overline{\phi}^z \overline{w}^x)_{i,k} \Delta x], \qquad (15)$$

where

$$\delta_x(\psi)_{i,k} \equiv \psi_{i+(1/2),k} - \psi_{i-(1/2),k}, \qquad (16)$$

$$\delta_z(\psi)_{i,k} \equiv \psi_{i,k+(1/2)} - \psi_{i,k-(1/2)}. \qquad (17)$$

The advection terms for momentum are also discretized in the same way. The second-order central difference scheme is used for pressure gradient terms and diffusion terms. Spatially discretized forms of Eqs. (1)–(4) for an uncut cell are therefore given as

$$\left(\frac{\partial \rho u}{\partial t}\right)_{i-(1/2),k-(1/2)} = -\frac{1}{V} [\delta_x (\overline{\rho}^z \overline{u}^x \overline{u}^x)_{i-(1/2),k-(1/2)} \Delta z$$
$$+ \delta_z (\overline{\rho}^x \overline{u}^z \overline{w}^z)_{i-(1/2),k-(1/2)} \Delta x]$$
$$- \frac{\delta_x (\overline{p'}^z)_{i-(1/2),k-(1/2)}}{\Delta x} + (D_u^*)_{i-(1/2),k-(1/2)}, \qquad (18)$$

$$\left(\frac{\partial \rho w}{\partial t}\right)_{i-(1/2),k-(1/2)} = -\frac{1}{V}[\delta_x(\overline{\rho}^z\overline{w}^x\overline{u}^x)_{i-(1/2),k-(1/2)}\Delta z + \delta_z(\overline{\rho}^x\overline{w}^z\overline{w}^z)_{i-(1/2),k-(1/2)}\Delta x] - \frac{\delta_z(\overline{p'}^x)_{i-(1/2),k-(1/2)}}{\Delta z}$$

$$- \overline{\overline{\rho'}^x}^z_{i-(1/2),k-(1/2)}g + (D_w^*)_{i-(1/2),k-(1/2)}, \tag{19}$$

$$\left(\frac{\partial p'}{\partial t}\right)_{i,k} = -\frac{c_p R}{c_v}\left(\frac{p_{i,k}}{p_0}\right)^{R/c_p}\frac{1}{V}[\delta_x(\overline{\rho\theta}^x\overline{u}^z)_{i,k}\Delta z$$

$$+ \delta_z(\overline{\rho\theta}^z\overline{w}^x)_{i,k}\Delta x - (D_\theta^*)_{i,k}], \tag{20}$$

$$\left(\frac{\partial \rho'}{\partial t}\right)_{i,k} = -\frac{1}{V}[\delta_x(\overline{\rho}^x\overline{u}^z)_{i,k}\Delta z + \delta_z(\overline{\rho}^z\overline{w}^x)_{i,k}\Delta x], \tag{21}$$

where D_u^*, D_w^*, and D_θ^* are discretized forms of the diffusion terms, and V is the cell volume equal to $\Delta x \Delta z$.

We will now describe how this technique is implemented in a situation where some of the cells are cut by the immersed boundary. As a staggered arrangement of the scalar variables and velocity components is used, the scalar and velocity cells are at different locations and are treated separately. No model solutions are computed for nodes completely inside the topography. First, let us discuss the discretization of conservation equations for scalar quantities on the scalar cell O enclosed by the area $\mathcal{ABCDE}$ (Fig. 4). The cell exchanges flux with the scalar cells N, E, W, and SW. Zero normal flow is assumed at the faces on the immersed boundary. Though we focus here on the case of a vertically combined cell, the spatial discretization on horizontally combined cells is also handled in the same way.

The surface integral of the flux on the top face $\mathcal{AE}$ is computed in the same way as for an uncut cell. The key issue here is to evaluate the integrals on the left and right faces. The integral on the right face $\mathcal{DE}$ can be approximated to second-order accuracy as

$$\int_{\mathcal{DE}} f\,dz \approx f_e \overline{\mathcal{DE}}, \tag{22}$$

where f_e is computed at the center of face $\mathcal{DE}$. In the case of face $\mathcal{AB}$, the flux through the face is composed of two fluxes: the flux exchanged with cell W and that exchanged with cell SW. Thus, the surface integral of the flux on face $\mathcal{AB}$ can be decomposed as

$$\int_{\mathcal{AB}} f\,dz = \int_{\mathcal{AP}} f\,dz + \int_{\mathcal{PB}} f\,dz. \tag{23}$$

A second-order approximation to this integral is obtained as

$$\int_{\mathcal{AB}} f\,dz \approx f_w\overline{\mathcal{AP}} + f_{sw}\overline{\mathcal{PB}}, \tag{24}$$

where f_w and f_{sw} are computed at the center of face segments $\mathcal{AP}$ and $\mathcal{PB}$, respectively.

The evaluation of f_e, f_w, and f_{sw} requires the value of the normal velocity and the advected scalar quantity on the face centers. The normal velocity of these fluxes is obtained by linear interpolation between the velocity values on the ends of each face. For example, the normal velocity of f_e is evaluated as

$$u_e = (u_\mathcal{D} + u_\mathcal{E})/2. \tag{25}$$

The normal velocity of f_w and f_{sw} on the combined face $\mathcal{AB}$ are given by

$$u_w = (u_\mathcal{A} + u_\mathcal{P})/2, \tag{26}$$

$$u_{sw} = (u_\mathcal{P} + u_\mathcal{B})/2, \tag{27}$$

respectively. The calculation of the velocity components on the immersed boundary, such as $u_\mathcal{B}$ and $u_\mathcal{D}$, and on the combined faces, such as $u_\mathcal{P}$, is described later.

The calculation of the scalar quantity on the face centers can be more complicated. In the case of Fig. 4, the scalar quantity in f_w is obtained properly by a simple linear approximation between neighboring cell centers as

$$\phi_w = (\phi_O + \phi_W)/2. \tag{28}$$

This is not the case for ϕ_{sw}, as one of the neighboring cell centers is in the solid and is absorbed. The evaluation of ϕ_e too is not simple because the face center does not coincide with the middle of neighboring cell centers. One way to obtain these values with high-order accuracy is to use a linear or quadratic extrapolation scheme near the immersed boundary. In this study, the simple average of cell center values of the cells exchanging fluxes approximates the advected quantity on cell faces for computational simplification:

$$\phi_{sw} = (\phi_O + \phi_{SW})/2, \tag{29}$$

$$\phi_e = (\phi_O + \phi_E)/2. \tag{30}$$

Note that this simplified calculation of advected quantities does not violate mass conservation. Although our method is only formally first order near the boundary, we have demonstrated numerically in the appendix that we obtain results that are still globally second-order
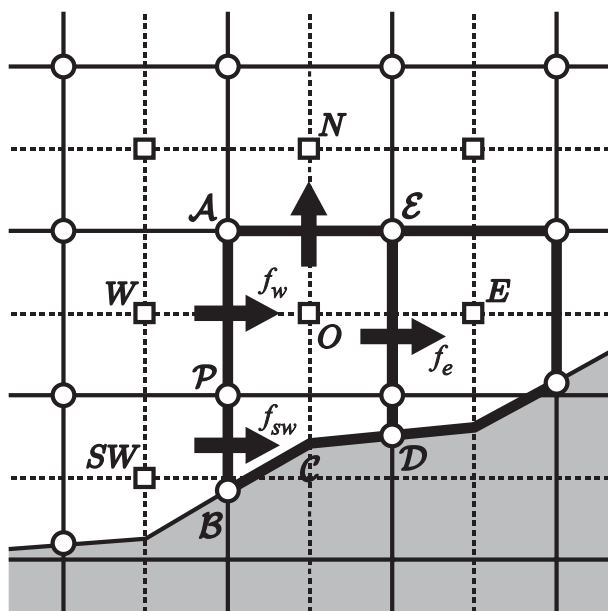
FIG. 4. Flux calculation on a scalar cell with the immersed boundary. Arrows indicate fluxes through the scalar cell O. Thick lines describe the boundaries of combined cells. Squares and circles represent scalar points and velocity points, respectively. Shaded region represents the topography in the model.
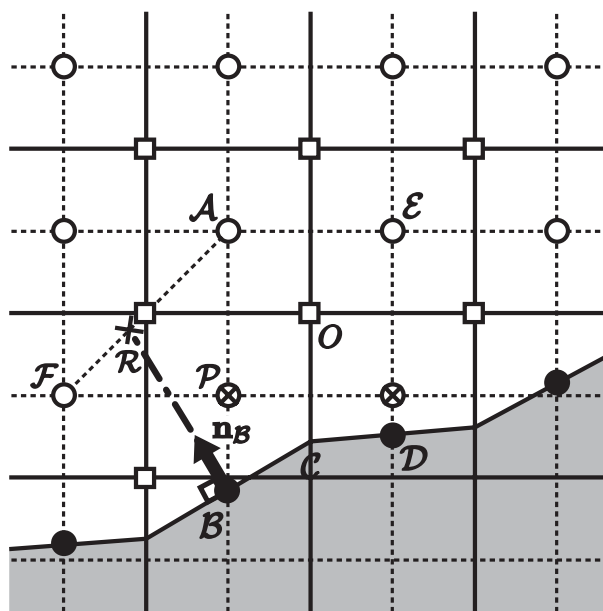

FIG. 5. Velocity cells corresponding to the scalar cells in Fig. 4. Squares represent scalar points. Open circles represent centers of velocity cells on which model solutions are predicted. Filled circles and crossed circles represent diagnosed velocity points on the immersed boundary and on the combined faces of the scalar cells, respectively. The dashed–dotted line and arrow describe the normal line and the unit normal direction to the surface at the boundary point $\mathcal{B}$, respectively. Shaded region represents the topography in the model.

accurate. As a result, the surface integrals of the flux on the left face $\mathcal{AB}$ and the right face $\mathcal{DE}$ are computed as

$$\int_{\mathcal{AB}} f \, dz \approx \phi_w u_w \overline{\mathcal{AP}} + \phi_{sw} u_{sw} \overline{\mathcal{PB}}, \tag{31}$$

$$\int_{\mathcal{DE}} f \, dz \approx \phi_e u_e \overline{\mathcal{DE}}, \tag{32}$$

respectively.

Now we consider the discretization of momentum equations on velocity cells. A key problem here is to accurately evaluate the pressure gradient at each velocity cell. In shaved cell model, however, it happens that some pressure points are under the terrain surface, and a velocity cell cut by the immersed boundary does not have necessary pressure points for the calculation of the pressure gradient. Ye et al. (1999) used an approach to express the pressure field near the immersed boundary in terms of a two-dimensional polynomial interpolating function and evaluate the pressure gradient based on this interpolating function under the no-slip boundary condition. In exchange for the systematic evaluation of the pressure gradient at cut cells of various shapes, it requires the evaluation of surface pressure which causes difficulties into GFD simulations.

The use of a staggered grid introduces another complexity into the discretization of momentum equations. On a nonstaggered grid, not only are the velocity components

and scalar variables collocated, but the position and geometry of the associated cells is also identical. With a staggered grid, the scalar and velocity cells are at different locations and will generally have a different shape when they are cut by the immersed boundary. In general, a cut cell scheme for a staggered grid must deal with this extra complexity (Kirkpatrick et al. 2003). When a cell-combining approach is introduced, in particular, another combining process for the velocity cells is normally required.

The current method provides a way around these complications by using the variable arrangement described in section 2b. For example, consider the velocity cells illustrated in Fig. 5, which correspond to the scalar cells in Fig. 4. In this method, the velocity on the immersed boundary and on the combined faces of the scalar cells, indicated by filled circles and crossed circles, respectively, are diagnostically evaluated. First, the velocity on the immersed boundary is calculated using the velocity boundary conditions. When the no-slip boundary condition is imposed, all the boundary velocity is set to zero. With the free-slip boundary condition, the component of the velocity that is tangential to the surface is preserved. If the unit normal direction to the surface at

a boundary point is **n**, the boundary velocity **v** is extrapolated as

$$\mathbf{v} = \tilde{\mathbf{v}} - (\tilde{\mathbf{v}} \cdot \mathbf{n})\mathbf{n}, \tag{33}$$

where $\tilde{\mathbf{v}}$ indicates the mean velocity above the normal direction that is computed from the velocities stored at open circled points surrounding the boundary point. For example, the velocity at the boundary point $\mathcal{B}$ is calculated as

$$\mathbf{v}_{\mathcal{B}} = \mathbf{v}_{\mathcal{R}} - (\mathbf{v}_{\mathcal{R}} \cdot \mathbf{n}_{\mathcal{B}})\mathbf{n}_{\mathcal{B}}, \tag{34}$$

where $\mathbf{n}_{\mathcal{B}}$ indicates the unit normal direction to the surface at the boundary point $\mathcal{B}$. In this case, the mean velocity is calculated at point $\mathcal{R}$ from the velocities at points $\mathcal{A}$ and $\mathcal{F}$ as

$$\mathbf{v}_{\mathcal{R}} = \mathbf{v}_{\mathcal{A}}(1 - \lambda_{\mathcal{R}}) + \mathbf{v}_{\mathcal{F}}\lambda_{\mathcal{R}}, \tag{35}$$

where the factor $\lambda_{\mathcal{R}}$ is defined as

$$\lambda_{\mathcal{R}} = \overline{\mathcal{A}\mathcal{R}}/\overline{\mathcal{A}\mathcal{F}}. \tag{36}$$

Then, the velocity at point $\mathcal{P}$ on the combined face $\mathcal{A}\mathcal{B}$ of the scalar cell O is calculated by assuming a linear distribution of velocity between $\mathcal{A}$ and $\mathcal{B}$ as

$$\mathbf{v}_{\mathcal{P}} = \mathbf{v}_{\mathcal{A}}(1 - \lambda_{\mathcal{P}}) + \mathbf{v}_{\mathcal{B}}\lambda_{\mathcal{P}}, \tag{37}$$

where the linear interpolation factor $\lambda_{\mathcal{P}}$ is defined as

$$\lambda_{\mathcal{P}} = \overline{\mathcal{A}\mathcal{P}}/\overline{\mathcal{A}\mathcal{B}}. \tag{38}$$

Momentum equations are solved only on the velocity cells with centers indicated by open circles, and all of them retain rectangular shapes (Fig. 5). Therefore, the calculation of fluxes through each cell face is quite straightforward. At the same time, the calculation of the pressure gradient at each cell is simply performed without the evaluation of surface pressure. Furthermore, there is also no need to combine velocity cells. Thus, the computational cost of combining cells is kept as low as that of nonstaggered models. Since the velocity cells only include the fully rectangular cells and do not enclose the entire fluid domain, momentum is not conserved in our model like many other models using a vertically staggered grid (e.g., Saito et al. 2001; Satoh 2002; Klemp et al. 2007). Our model also does not conserve kinetic energy, although mass conservation is guaranteed. Though this paper focuses only on two-dimensional applications, the overall methodology described here is in principle extendable to three dimensions.

3. Numerical examples of mountain waves

This section presents the results of test simulations of flows passing over four different mountains. Every test involves a mountain located at the center of the lower boundary. The following atmospheric and boundary conditions are imposed on all the simulations. A constant horizontal velocity, $U = 10$ m s^{-1}, is initially imposed on the entire domain. The constant Brunt–Väisälä frequency is $N = 0.01$ s^{-1}. The lower and lateral boundary conditions are free slip and cyclic, respectively. The number of grid points in the horizontal dimension is 2000, which prevents cyclic lateral boundaries from contaminating the simulated results. The height of the domain is 25 km, and a sponge layer (Klemp and Lilly 1978) is placed higher than 15 km to avoid reflecting the gravity wave at the rigid top boundary.

The leapfrog scheme with the Asselin filter (Asselin 1972) is used for time integration. A fourth-order artificial diffusion term is introduced in both the horizontal and vertical directions to suppress numerical noise. For cells without necessary neighboring fluid points for the calculation of the fourth-order term, a second-order artificial diffusion term is introduced, where boundary conditions are used at mountain surfaces. When appropriate boundary conditions cannot be obtained, no artificial diffusion term is used for cells just above the surface.

a. Flow over a bell-shaped mountain

The first test examines the accuracy of the model by simulating flow over a bell-shaped low mountain with gentle slopes. The topographic height $h(x)$ is assumed to be

$$h(x) = \frac{h_m}{1 + (x/a)^2}, \tag{39}$$

where h_m is the height of the mountain top, and a is the half-width of the mountain. Here $h_m = 100$ m and $a = 5$ km are used. The nondimensional mountain height scaled by the Scorer parameter, Nh_m/U, is 0.1. Thus, the linear theory is well applicable in this case. The horizontal and vertical resolutions are 1 km and 50 m, respectively. As the slope is gentle enough, only vertical combinations are used in this test.

Figures 6a and 6b show vertical velocity fields over the bell-shaped mountain calculated by Sayaca-2D and linear theory, respectively. The vertical velocity calculated by the model agrees well with that by the linear theory. The momentum flux in Sayaca-2D normalized by that in the linear theory is shown in Fig. 6c. It is nearly unity from near the surface to 10 km. Thus, the momentum flux in the model agrees well with that of the linear theory. The lack of momentum and energy conservation of our model is not considered to introduce serious error into the simulated flow because total momentum and
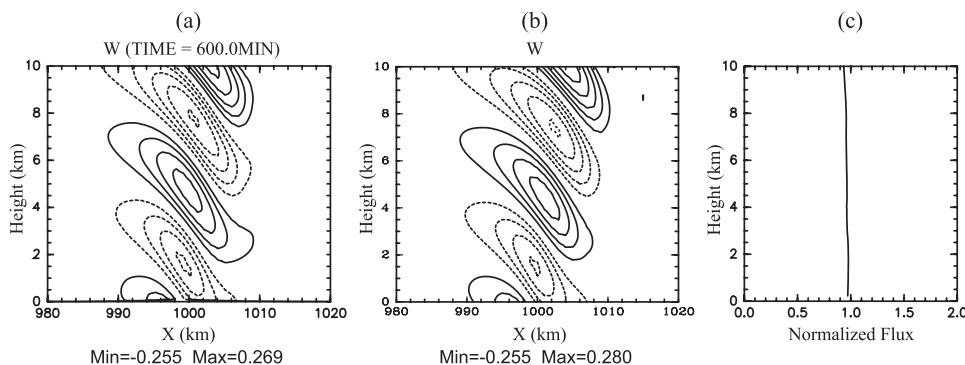
FIG. 6. Results over the bell-shaped mountain. (a) Vertical velocity reproduced by Sayaca-2D. (b) Vertical velocity in the linear theory. (c) Simulated momentum flux by Sayaca-2D normalized by the linear theoretical value. The contour interval in (a) and (b) is 0.05 m s^{-1}. The integration time in (a) and (c) is 600 min. Solid and dashed lines indicate positive and negative values, respectively.

total energy increased only about 0.12% and about 0.26%, respectively, during the 10-h time integration. These results lead to the conclusion that Sayaca-2D reproduces a sufficiently accurate flow over gentle slopes, and in particular that vertical combinations of cells in our model work properly.

b. Flow over a pyramidal mountain

The presented cell-combining method switches the direction of combination between the vertical direction and the horizontal direction at a slope angle $|\sigma| = \tan^{-1}(\Delta z/\Delta x)$. To show that horizontal combinations of cells work as effectively as vertical combinations, the following two physically identical simulations are performed using a pyramidal mountain with $|\sigma| = \tan^{-1}(\Delta z/\Delta x)$. One uses only vertical combinations (Fig. 7a), and the other uses only horizontal combinations (Fig. 7b) for the same pyramidal mountain. Here, $\Delta x = 500$ m and $\Delta z = 200$ m are used. The slope angle is 20.8°.

Figures 8a and 8b show the simulated vertical velocity fields corresponding to Figs. 7a and 7b, respectively. Clearly, the results of the two simulations are practically

the same. The several differences between two results near the surface appear to be acceptable because this test uses grids that are rather coarse and largely different shapes. Thus, we conclude that horizontal combinations in our model work properly as well as vertical combinations.

c. Flow over a semicircular mountain

This test demonstrates the ability of the model to simulate flow over topography including both gentle and steep slopes, where significant errors are observed in models using terrain-following coordinates. Here a semicircular mountain of radius $r = 1$ km is used as in Satomura (1989) and Yamazaki and Satomura (2008).

Figures 9a and 9b show the vertical velocity fields calculated by Sayaca-2D and the terrain-following model developed by Satomura (1989), respectively. Here, both the horizontal and vertical grid intervals are 500 m. Referring to the smooth streamlines of the analytical solution given by Miles and Huppert (1968) and the result from the model using general curvilinear coordinates shown in Fig. 3 of Satomura (1989), discontinuities appeared just
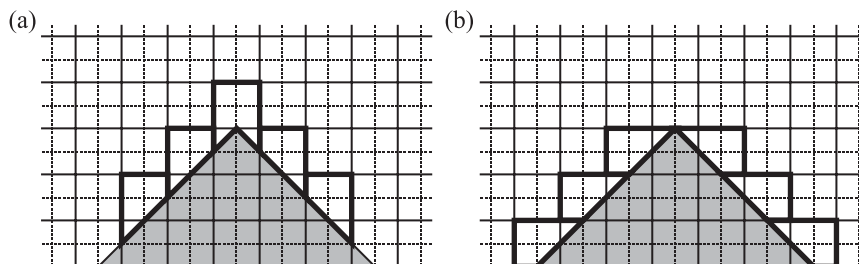

FIG. 7. Scalar cell configurations of comparative simulations over a pyramidal mountain. Thick lines describe the boundaries of combined cells. Shaded region represents the topography in the model. (a) Only vertical combinations are used. (b) Only horizontal combinations are used.
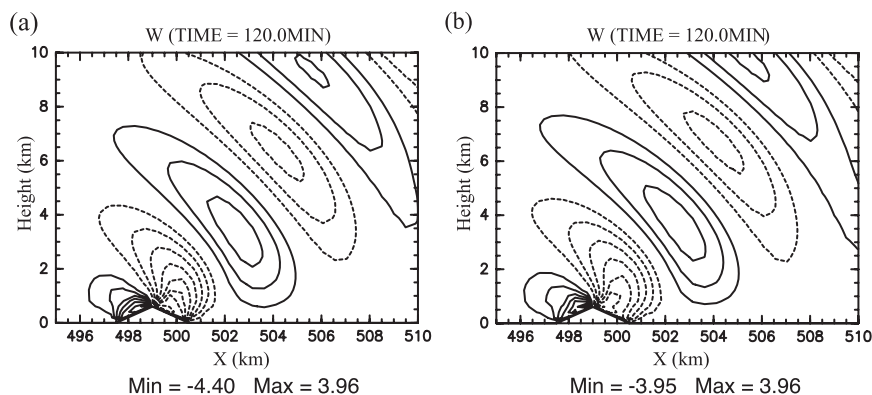
FIG. 8. The vertical velocity over the pyramidal mountain after 120 min of integration (a) by the model using vertical combinations only and (b) by the model using horizontal combinations only. The contour interval is 0.5 m s^{-1}. Solid and dashed lines indicate positive and negative values, respectively.

above the mountain in Fig. 9b are spurious vertical velocity modes, and disappear in Fig. 9a. The near-surface amplitude in Fig. 9a, however, is much smaller than that in the general curvilinear model. To investigate the cause of small amplitude near the surface, the same test with higher resolution is performed by Sayaca-2D. In this case, horizontal and vertical grid intervals are halved to 250 m. The simulated vertical velocity is shown in Fig. 10. Since the near-surface amplitude in Fig. 10 is as large as that in Fig. 3 of Satomura (1989), it seems reasonable to suppose that the small amplitude in Fig. 9a results from cell combinations that nearly double the size of cells near the surface. We therefore conclude that Sayaca-2D reproduces accurate and physically reasonable flows over the mountain including both gentle and steep slopes. At the same time, it is proved that Sayaca-2D works properly

even when horizontally combined cells and vertically combined cells coexist.

d. Flow over a cliff

As described in section 1, the method in Yamazaki and Satomura (2008) uses only vertical combinations and may form vertically long combined cells along extremely steep slopes that seriously reduce resolution. In this test, we demonstrate that the use of horizontal combinations in this paper resolves this problem and improves the results of flow over extremely steep slopes. Here two physically identical simulations are performed using a cliff shown in Fig. 11: one uses only vertical combinations (Fig. 11a) and the other uses only horizontal combinations (Fig. 11b) for the same cliff. The
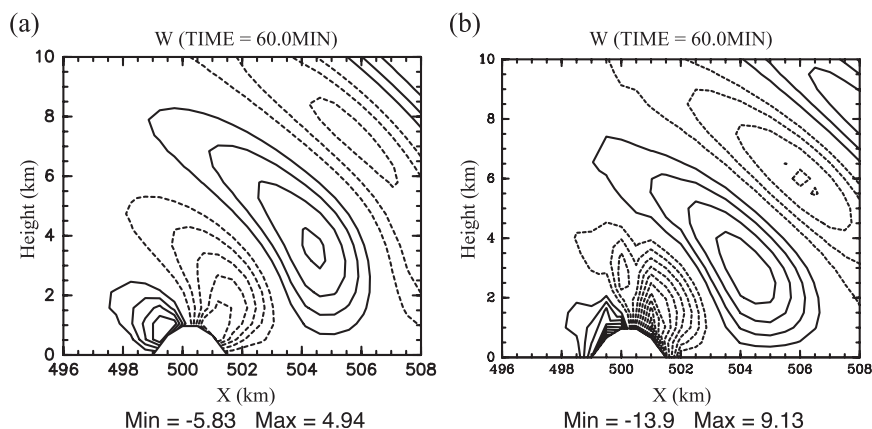

FIG. 9. The vertical velocity over the semicircular mountain after 60 min of integration (a) by Sayaca-2D, and (b) by the terrain-following model. The horizontal and vertical resolutions are both 500 m. The contour interval is 1 m s^{-1}. Solid and dashed lines indicate positive and negative values, respectively.
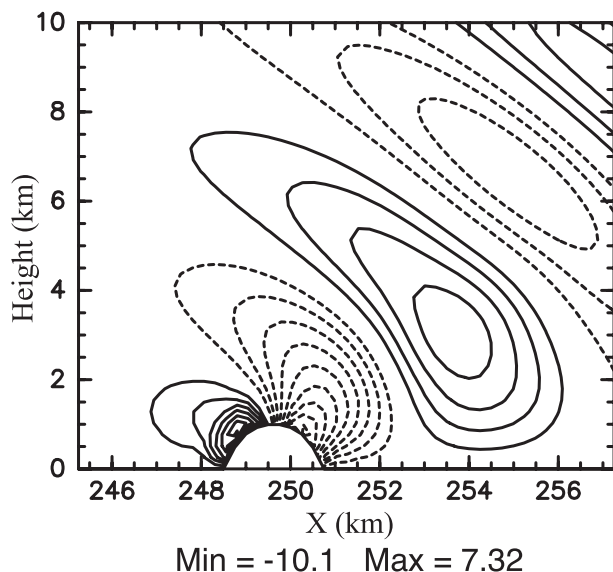
FIG. 10. As in Fig. 9a, but that horizontal and vertical resolutions are both 250 m.

height of the mountain h_m = 1.73 km, thus Nh_m/U = 1.73. Both horizontal and vertical resolutions are 288.3 m. The slope angle is 80.5°.

Figures 12a and 12b show the simulated potential temperature fields corresponding to Figs. 11a and 11b, respectively. Referring to the analytical solution of flow over a thin barrier for Nh_m/U = 1.73 (Huppert and Miles 1969), the experiment with horizontal combinations successfully reproduces flow over the cliff, while the result with vertical combinations is clearly different

from the analytical solution. This test therefore proves the advantage of the current method over the method in Yamazaki and Satomura (2008) for extremely steep terrain.

4. Conclusions

To achieve high-resolution and highly precise simulations over steep topography, a new two-dimensional nonhydrostatic atmospheric model code-named Sayaca-2D was developed using the shaved cell method. To avoid severe restriction on time steps maintaining the exact evaluation of cut cell volumes, combined cells are used in both the horizontal and vertical directions. A unique staggered arrangement of variables was devised that leads to the following characteristics suitable for GFD simulations: 1) pressure gradient computations near the immersed boundary are clear and greatly simplified, 2) velocity boundary conditions can be simply imposed by direct evaluation of the velocity on the boundary, and 3) the computational cost of combining cells is held down as low as that of nonstaggered models.

The accuracy of Sayaca-2D was confirmed by simulating flow over a gently sloping bell-shaped low mountain and comparing the result with the analytical solution given by the linear theory. As the presented method uses both horizontal and vertical combinations depending on slope angles, comparative simulations over the same pyramidal mountain were carried out to confirm that the two combinations produce consistent results. The ability of the model to simulate flow over topography including
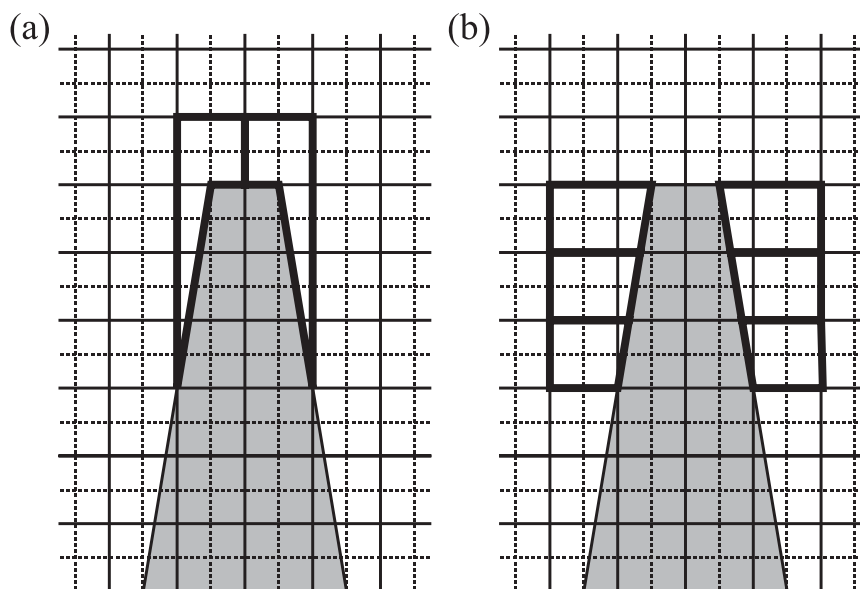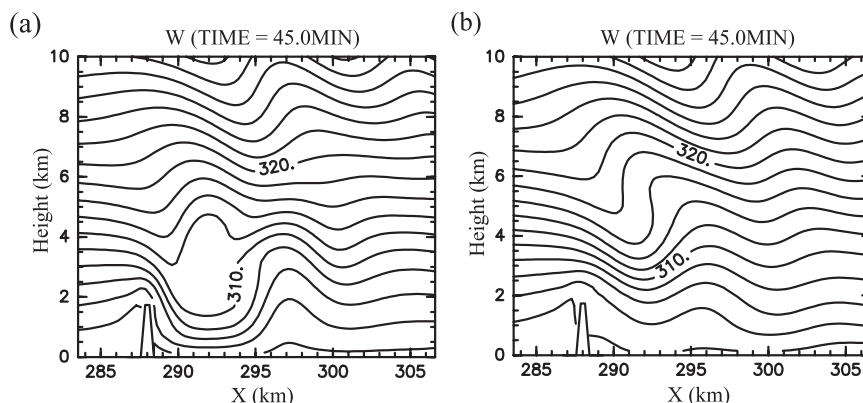

FIG. 11. As in Fig. 7, but over a cliff.

FIG. 12. The potential temperature over the cliff after 45 min of integration (a) by the model using vertical combinations only and (b) by the model using horizontal combinations only. The contour interval is 2 K.

both gentle and steep slopes was demonstrated using a semicircular mountain. Sayaca-2D reproduces quite smooth and physically reasonable flows over the semicircular mountain, while large errors are observed in a model using commonly used terrain-following coordinates, thereby demonstrating the advantage of the current method over the methods using terrain-following coordinates for flows over steep terrain. Finally, the test of flow over a cliff with the slope angle of 80.5° was performed and showed that the use of horizontal cell combination clearly improves the results of flow over extremely steep slopes compared to those using vertical combinations.

The extension of our model to three dimensions should be straightforward. The presented arrangement of variables would enable simple cut cell computations in three dimensions as well as in two dimensions. For establishing the shape and position of a three-dimensional orographic surface, we will use a series of two-dimensional bilinear surfaces (Steppeler et al. 2006; Lock 2008). However, these extensions have not yet been implemented or tested in our model.

A remaining critical issue in using Cartesian coordinates is that a number of model levels are required to obtain high near-ground vertical resolution over a wide range of topographic heights. The main new challenge is keeping the overall fine prospect of parallelization of the model code on next-generation supercomputers, while obtaining sufficient vertical resolution near the ground. Further work is intended to solve this issue as well as to extend the code to three dimensions.

APPENDIX

Estimation of Global Accuracy

In this section, we numerically demonstrate that our method is practically second-order accurate for a flow over
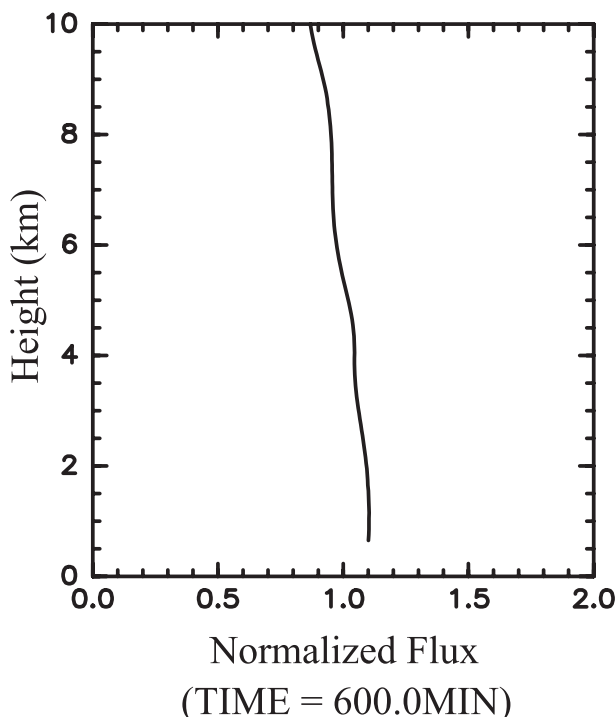

Normalized Flux
(TIME = 600.0MIN)

FIG. A1. Simulated momentum flux by Sayaca-2D after 600 min of integration normalized by the theoretical value for nonlinear mountain waves.
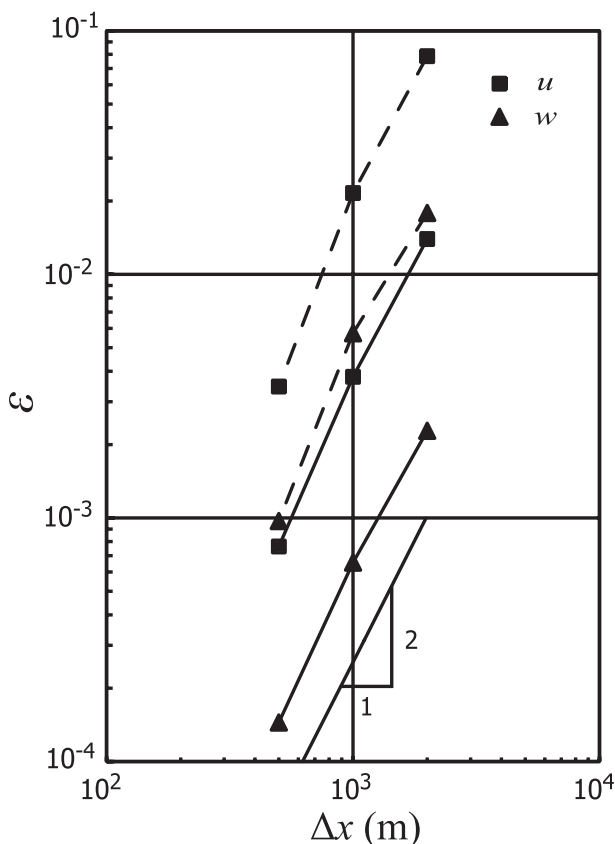
FIG. A2. Variation of global error in u and w with horizontal grid intervals for flow over the bell-shaped mountain. Solid and dashed lines indicate L_1 and L_2 norms of the errors, respectively.

Then, both the L_1 and L_2 norms of the global errors are computed by assuming the result with $\Delta x = 250$ m as the exact solution as

$$\varepsilon_{L_1} = \frac{1}{N_x N_z} \sum_{j=1}^{N_x N_z} |\psi_j^{\text{numerical}} - \psi_j^{\text{exact}}| \quad \text{and}$$

$$\varepsilon_{L_2} = \left[\frac{1}{N_x N_z} \sum_{j=1}^{N_x N_z} (\psi_j^{\text{numerical}} - \psi_j^{\text{exact}})^2 \right]^{1/2}, \quad \text{(A1)}$$

where N_x and N_z indicate the horizontal and vertical grid number bellow the sponge layer, respectively. We show a log–log plot of the errors in both velocity components u and w versus horizontal grid intervals in Fig. A2. Also shown is a line with a slope of 2 that corresponds to the second-order accurate convergence. The plot shows that the global error in our computed solution decreases in a manner consistent with a second-order accurate scheme. This test therefore proves that our method produces results of global second-order accuracy.

REFERENCES

Adcroft, A., C. Hill, and J. Marshall, 1997: Representation of topography by shaved cells in a height coordinate ocean model. *Mon. Wea. Rev.*, **125**, 2293–2315.

Arakawa, A., and V. R. Lamb, 1977: Computational design of the basic dynamical processes of the UCLA general circulation model. *Methods Comput. Phys.*, **17**, 173–265.

Asselin, R., 1972: Frequency filter for time integrations. *Mon. Wea. Rev.*, **100**, 487–490.

Bryan, K., 1969: A numerical method for the study of the circulation of the world ocean. *J. Comput. Phys.*, **4**, 347–376.

Calhoun, D., and R. J. LeVeque, 2000: A Cartesian grid finite-volume method for the advection-diffusion equation in irregular geometries. *J. Comput. Phys.*, **157**, 143–180.

Durran, D. R., and J. B. Klemp, 1983: A compressible model for the simulation of moist mountain waves. *Mon. Wea. Rev.*, **111**, 2341–2361.

Gallus, W. A., and J. B. Klemp, 2000: Behavior of flow over step orography. *Mon. Wea. Rev.*, **128**, 1153–1164.

Huppert, H. E., and J. W. Miles, 1969: Lee waves in a stratified flow. Part 3: Semi-elliptical obstacle. *J. Fluid Mech.*, **35**, 481–496.

Janjić, Z. I., 1989: On the pressure gradient force error in σ-coordinate spectral models. *Mon. Wea. Rev.*, **117**, 2285–2292.

Kirkpatrick, M. P., S. W. Armfield, and J. H. Kent, 2003: A representation of curved boundaries for the solution of the Navier–Stokes equations on a staggered three-dimensional Cartesian grid. *J. Comput. Phys.*, **184**, 1–36.

Klemp, J. B., and D. K. Lilly, 1978: Numerical simulation of hydrostatic mountain waves. *J. Atmos. Sci.*, **35**, 78–107.

——, and R. B. Wilhelmson, 1978: The simulation of three-dimensional convective storm dynamics. *J. Atmos. Sci.*, **35**, 1070–1096.

——, W. C. Skamarock, and J. Dudhia, 2007: Conservative split-explicit time integration methods for the compressible non-hydrostatic equations. *Mon. Wea. Rev.*, **135**, 2897–2913.

terrain. This test uses a bell-shaped mountain with the height $h_m = 400$ m and the half-width $a = 10$ km. Here four different horizontal grid intervals: $\Delta x = 2$ km, 1 km, 500 m, and 250 m are used. The errors are calculated by assuming the solution with $\Delta x = 250$ m as the exact solution. To save computational time, the vertical grid interval is fixed at 200 m for all the simulations. The same atmospheric and boundary conditions used in section 3 are imposed. In this case, the nonlinear effects should be significant than in section 3a because $N h_m / U = 0.4$.

First, to verify the result with $\Delta x = 250$ m, we follow the procedure used by Durran and Klemp (1983) and Xue et al. (2000) and determine a mountain profile so that the model solution including nonlinear effects follows the linear solution forced by this new profile at the lower boundary. For a bell-shaped mountain originally 400 m high, the resultant mountain has a height of 415.7 m. The momentum flux scaled by that for linear waves with $h_m = 415.7$ m in the experiment using $\Delta x = 250$ m is plotted in Fig. A1. It is nearly constant, therefore it would be possible to use the result as a proxy of the exact solution.

Lock, S.-J., 2008: Development of a new numerical model for studying microscale atmospheric dynamics. Ph.D. thesis, University of Leeds, 158 pp.

Mesinger, F., Z. I. Janjic, S. Nickovic, D. Gavrilov, and D. G. Deaven, 1988: The step-mountain coordinate: Model description and performance for cases of Alpine lee cyclogenesis and for a case of an Appalachian redevelopment. *Mon. Wea. Rev.,* **116,** 1493–1518.

Miles, J. W., and H. E. Huppert, 1968: Lee waves in a stratified flow. Part 2: Semi-circular obstacle. *J. Fluid Mech.,* **33,** 803–814.

Mittal, R., and G. Iaccarino, 2003: Immersed boundary methods. *Annu. Rev. Fluid Mech.,* **37,** 239–261.

——, C. Bonilla, and H. S. Udaykumar, 2003: Cartesian grid methods for simulating flows with moving boundaries. *Computational Methods and Experimental Measurements XI,* C. A. Brebbia, G. M. Carlomagno, and P. Anagnostopoulos, Eds., WIT Press, 557–566.

Saito, K., T. Kato, H. Eito, and C. Muroi, 2001: Documentation of the Meteorological Research Institute/Numerical Prediction Division unified nonhydrostatic model. Tech. Rep. 42, Meteorological Research Institute, 133 pp.

Satoh, M., 2002: Conservative scheme for the compressible nonhydrostatic models with the horizontally explicit and vertically implicit time integration scheme. *Mon. Wea. Rev.,* **130,** 1227–1245.

Satomura, T., 1989: Compressible flow simulations on numerically generated grids. *J. Meteor. Soc. Japan,* **67,** 473–482.

——, and S. Akiba, 2003: Development of high-precision nonhydrostatic atmospheric model (1): Governing equations. *Ann. Disaster Prev. Res. Inst. Kyoto Univ.,* **46B,** 331–336. [Available online at http://www.dpri.kyoto-u.ac.jp/dat/nenpo/no46/46b0/a46b0t32.pdf.]

Schär, C., D. Leuenberger, O. Fuhrer, D. Lüthi, and C. Girard, 2002: A new terrain-following vertical coordinate for atmospheric prediction models. *Mon. Wea. Rev.,* **130,** 2459–2480.

Semtner, A. J., and Y. Mintz, 1977: Numerical simulation of the Gulf Stream and midocean eddies. *J. Phys. Oceanogr.,* **7,** 208–230.

Steppeler, J., H. W. Bitzer, M. Minotte, and L. Bonaventura, 2002: Nonhydrostatic atmospheric modeling using a z-coordinate representation. *Mon. Wea. Rev.,* **130,** 2143–2149.

——, and Coauthors, 2006: Prediction of clouds and rain using a z-coordinate nonhydrostatic model. *Mon. Wea. Rev.,* **134,** 3625–3643.

Sundqvist, H., 1976: On vertical interpolation and truncation in connection with use of sigma system models. *Atmosphere (Toronto),* **14,** 37–52.

Thompson, J. F., Z. U. A. Warsi, and C. W. Mastin, 1985: *Numerical Grid Generation: Foundations and Applications.* Elsevier Science, 483 pp.

Thuburn, J., and T. J. Woollings, 2005: Vertical discretizations for compressible Euler equation atmospheric models giving optimal representation of normal modes. *J. Comput. Phys.,* **203,** 386–404.

Tomita, H., and M. Satoh, 2004: A new dynamical framework of nonhydrostatic global model using the icosahedral grid. *Fluid Dyn. Res.,* **34,** 357–400.

Tseng, Y.-H., and J. H. Ferziger, 2003: A ghost-cell immersed boundary method for flow in complex geometry. *J. Comput. Phys.,* **192,** 593–623.

Udaykumar, H. S., W. Shyy, and M. M. Rao, 1996: A mixed Eulerian-Lagrangian method for fluid flows with complex and moving boundaries. *Int. J. Numer. Methods Fluids,* **22,** 691–712.

——, R. Mittal, P. Rampunggoon, and A. Khanna, 2001: A sharp interface Cartesian grid method for simulating flows with complex moving boundaries. *J. Comput. Phys.,* **174,** 345–380.

Walko, R. L., and R. Avissar, 2008: The Ocean–Land–Atmosphere Model (OLAM). Part II: Formulation and tests of the nonhydrostatic dynamic core. *Mon. Wea. Rev.,* **136,** 4045–4062.

Xue, M., K. K. Droegemeier, and V. Wong, 2000: The advanced regional prediction system (ARPS)—A multi-scale nonhydrostatic atmospheric simulation and prediction model. Part I: Model dynamics and verification. *Meteor. Atmos. Phys.,* **75,** 161–193.

Yamazaki, H., and T. Satomura, 2008: Vertically combined shaved cell method in a z-coordinate nonhydrostatic atmospheric model. *Atmos. Sci. Lett.,* **9,** 171–175, doi:10.1002/asl.187.

Ye, T., R. Mittal, H. S. Udaykumar, and W. Shyy, 1999: An accurate Cartesian grid method for viscous incompressible flows with complex immersed boundaries. *J. Comput. Phys.,* **156,** 209–240.

Zängl, G., 2002: An improved method for computing horizontal diffusion in a sigma-coordinate model and its application to simulations over mountainous topography. *Mon. Wea. Rev.,* **130,** 1423–1432.

——, 2003: A generalized sigma-coordinate system for the MM5. *Mon. Wea. Rev.,* **131,** 2875–2884.